Available online at www.sciencedirect.com
ScienceDirect
ELSEVIER
International Journal of Heat and Fluid Flow 28 (2007) 1360–1378
International Journal of HEAT AND FLUID FLOW
www.elsevier.com/locate/ijhff

Large-eddy simulations of flow over a jet-impinged wall-mounted cube in a cross stream

M. Popovac *, K. Hanjalić [1]

Department of Multi-scale Physics, Faculty of Applied Sciences, Delft University of Technology, Lorentzweg 1, 2628 CJ Delft, Netherlands

Received 4 March 2007; received in revised form 16 May 2007; accepted 23 May 2007
Available online 16 July 2007

Abstract

We report on large-eddy simulations of flow over a heated, jet-impinged, wall-mounted cube in a cross-flow, representing a simplified case of electronics cooling. The configuration consists of an in-line array of five cubes mounted on the bottom wall of a plane channel. The central heated cube is cooled by two mutually perpendicular streams of air: a channel flow at $Re_c = 4800$ and a round impinging jet $Re_j = 5200$ issued from an orifice in the opposite upper channel wall. The study was aimed at investigating flow structures and turbulence statistics, as well as their thermal signature and heat transfer on the cube surface. The comparison with measurement in a similar, though not identical, configuration shows qualitatively good agreement despite some important differences in flow conditions. The paper outlines the method applied and presents a selection of results.
© 2007 Elsevier Inc. All rights reserved.

Keywords: LES; Wall-mounted heated cubes; Jet in a cross-flow; Impinging jet; Electronic cooling

---

1. Introduction

In many industrial applications local overheating is the main cause of a device or equipment failure and the major limitation to further increase in their power and efficiency. The problem is especially acute in electronics industry where chips and other components require intensive cooling in order to ensure reliable long-term operation. According to Moore's law (Moore, 1965), the power of each new generation of microprocessors doubles, and so does their heat dissipation rate. In addition to the general problem of removing highly concentrated heat, the main obstacles in further power increase and size miniaturization of computer processors are the local hot spots, which can cause local overheating and thermal fatigue. Similar problems are encountered in the internal and external cooling of gas-turbine blades, where effective heat removal is the chief barrier to increasing the turbine inlet temperature needed for improving the overall efficiency of the gas-turbine cycle. In both above mentioned and numerous other examples, the understanding and accurate prediction of the local temperature and heat transfer is the key prerequisite for the successful design and reliable operation of different kinds of devices, as well as for their further development beyond the present limits.

We present here an analysis of the flow pattern, turbulence structure and its statistics, and wall heat transfer in a configuration relevant to cooling of electronic devices. The aim is to gain a better insight into the flow structures and their correlation with the local heat transfer. To this purpose, we performed LES study of fluid flow and conjugate heat transfer in a configuration that mimics a realistic electronics cooling. The configuration considered consists of an in-line row of five cubes mounted on the lower wall in a plane channel flow, where the central, internally-heated, cube was subjected to an impinging round jet

---

* Corresponding author. Present address: Laboratory for Aero and Hydrodynamics, 3mE Faculty, Delft University of Technology, Leeghwaterstraat 21, 2628 CA, Delft, Netherlands.
E-mail address: M.Popovac@tudelft.nl (M. Popovac).

[1] Present address: Marie Curie Chair, Dipartimento di Meccanica ed Aeronautica, University of Rome 'La Sapienza', Via Eudussiana 18, 00184 Rome, Italy.

0142-727X/$ - see front matter © 2007 Elsevier Inc. All rights reserved.
doi:10.1016/j.ijheatfluidflow.2007.05.009

issuing from an orifice in the opposite channel wall. This configuration is a close replica (not identical, though) of the experiment of Tummers et al. (2005) in which detailed particle-image velocimetry (PIV) and infrared thermography measurements were reported. More details on the numerical flow analysis can be found in Popovac (2006). In essence, these simulations are a follow-up and a synthesis of the earlier LES of flow over a heated wall-mounted heat cube in a matrix in a similar channel but without a jet (Ničeno, 2001; Ničeno et al., 2002; Ničeno and Hanjalić, 2005) and of a round jet impinging normally on a heated flat plate (Hadžiabdić, 2006; Hadžiabdić and Hanjalić, submitted for publication). It is noted that RANS calculations of the flow and heat transfer for similar configuration, with one cube only and with the jet impinging centrally on the cube, have been reported by Rundström and Moshfegh (2006).

2. Flow configuration and computational details

The sketch of the flow under consideration and its dimensions are shown in Fig. 1. It consists of two fluid streams: the first is a channel flow over an in-line row of five wall-mounted cubes denoted by $C1$ to $C5$, and the second is a round jet impinging normally onto the (only heated) central cube $C3$, issued from an orifice that connects the channel and the top plenum chamber. The Reynolds number of the channel flow, based on its bulk velocity $U_c = 2.4$ m/s and the channel hight $2h = 30$ mm, is $Re_c = 4800$. A similar value has the jet Reynolds number $Re_j = 5200$, based on its bulk velocity $U_j = 6.5$ m/s and the diameter of the orifice $D = 12$ mm. An important parameter that governs the flow pattern of this configuration and a jet in the cross-flow in general, is the velocity ratio $\alpha_v = U_j/U_c = 2.7$. These Reynolds numbers and velocity ratio correspond roughly to real electronics cooling systems.

The configuration and flow parameters were chosen to resemble closely the experimental conditions reported by Tummers et al. (2005). The principal geometry dimension is the height of the cube $h = 15$ mm. The height of the channel is $H = 2h$, and the distance between the cube centres is $d = 4h$. The diameter of the orifice $D = 0.8h$, which gives the jet length-to-diameter ratio $h/D = 1.25$. The thickness of the wall that separates the channel from the plenum chamber, i.e. the length of the orifice is $n = 0.4h$. The dimensions of the domain and its elements, sketched in Fig. 1, are summarised in Table 1, but it should be noted that the simulations have been performed for a scaled geometry of the size normalised with h and the viscosity was adjusted to keep the specified Reynolds number. The flow characteristics are summarised in Table 2.

The spanwise channel width in the experimental setup was $W' = 20h$, making it possible to neglect all the effects of the side walls on the flow around the cubes. In the simulations this width was reduced to $W = 7h$ in order to rationalize the computational mesh, and the test simulations with a larger width indeed showed no noticeable influence of the side walls on the flow around the central cube. The top plenum chamber in the experiments was wide enough to eliminate any effects of the side walls on the jet formation in the orifice. In the simulations, again

Table 1
Dimensions of the computational domain are taken from the experiment, apart from the total length and width, which are taken somewhat shorter

Dimension		Value	
h	Height of the cube	$1h$	15 mm
H	Height of the channel	$2h$	30 mm
S	Cube centre to orifice axis shift	$0.5h$	7.5 mm
d	Centre-to-centre distance	$4h$	60 mm
D	Diameter of the orifice	$0.8h$	12 mm
n	Height of the orifice	$0.4h$	6 mm
δ	Thickness of the epoxy layer	$0.1h$	1.5 mm
W	Width of the channel	$7h$	105 mm

Table 2
Flow characteristics of the channel flow and the round impinging jet

	Channel flow	Impinging jet	Unit
Bulk velocity U	2.4	6.5	m/s
Mass flow rate $\dot{m}$	2.5×10^{-2}	8.5×10^{-4}	kg/s
Reynolds number Re	4800	5200	–
Velocity ratio α_v	2.7		–

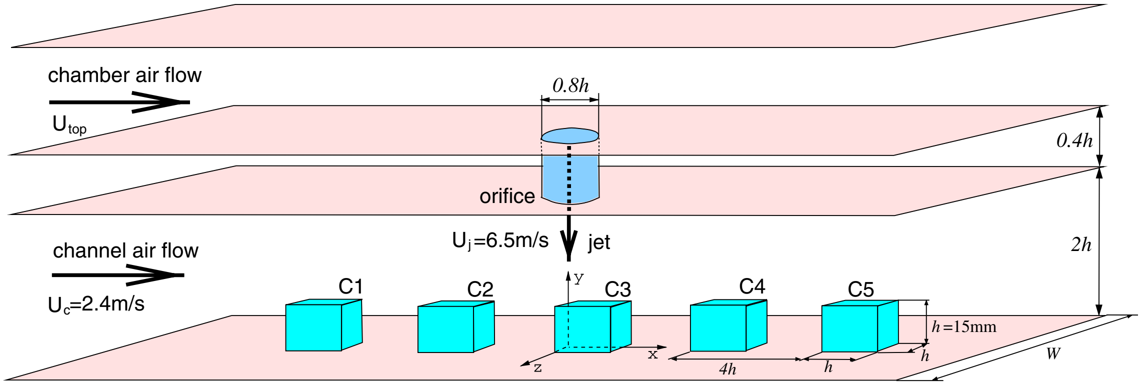

Fig. 1. Sketch of the experimental setup with dimensions ($h = 15$ mm), coordinate system and bulk velocities of the lateral flow and the jet.

for the sake of mesh economy, the top chamber was closed with walls with a hight of $4D$ and a width of $4D \times 4D$. Such a closed chamber was considered to be large enough to mimic the open chamber from the experiment, and ignore any influence of the side walls on the jet formation.

However, there is another small difference between the experimental setup and the numerical configuration, which appeared to have some influence. Namely, in the experiment of Tummers et al. (2005) the axis of the orifice from which the jet issues is shifted by 8 mm ($S' = 0.53h$) upstream from the centre of the cube $C3$, because in their preliminary measurements of the heat dissipation for various jet locations this jet positioning appeared to be optimal for achieving the maximum cooling effect. Yet, in order to make the mesh generation somewhat easier, in the numerical simulations the axis of the orifice was aligned with the leading edge of the central cube $C3$, i.e. the orifice is shifted back by 7.5 mm ($S = 0.5h$) upstream from the centre of $C3$. For this reason the origin of the coordinate system is also placed where the axis of the orifice intersects with the bottom wall, as shown in Fig. 1. This small difference between the computational and the experimental settings, originally considered as unimportant, appeared to cause some discrepancies in the obtained results, as discussed below.

2.1. Numerical and model parameters

Large-eddy simulations were performed using the in-house unstructured collocated finite volume CFD code *T-FlowS* (Ničeno and Hanjalić, 2005). The dynamic Smagorinsky procedure (Germano et al., 1991) was used for the calculation of the subgrid-scale stresses, and the turbulent heat fluxes were calculated as a passive scalar using the same dynamic approach (as explained by Calmet and Magnaudet (1996) among others). Therefore there was no need to specify a priori the Smagorinsky constant, nor to introduce any artificial near-wall damping of the subgrid-scale model. For the convective scheme, a full central differencing was used, and no problems with the numerical stability have been observed. However, in the iterative procedure the transport equations have been under-relaxed: for the momentum equation an under-relaxation factor of 0.9 was used, while for the pressure correction equation 0.8 was applied. The time marching was performed using a fully-implicit three-level time scheme. An iterative pressure correction algorithm was used for the pressure–velocity coupling, and the diagonally preconditioned conjugate gradient method was used for solving the linearised system of equations. The time step, normalised with the cube height and fluid viscosity, was set to $\Delta t_{\mathrm{nor}} = \nu \Delta t / h^2 = 1.33 \times 10^{-6}$. This gave a typical CFL number around 0.7, and only in isolated regions of high velocity CFL reached a peak value around 2.

In the separate channel flow simulation, ran simultaneously to generate the inflow data, the pressure drop was recalculated after each time step from the difference between the imposed mass flux $\dot{m}_0$ and the currently calculated $\dot{m}_1$. This resulted in a small variation of the Reynolds number of the computed flow: $\Delta Re/Re \approx 1\%$.

In the first $4t_{\mathrm{ft}}$, where $t_{\mathrm{ft}} = h/U_{\mathrm{j}}$ is the flow-through time based on the bulk velocity of the jet and the height of the cube, the statistics was not gathered in order to let the flow structures develop naturally. After that the results were averaged over the normalised averaging time $t_{\mathrm{nor}} = 1.5 \times 10^{-2}$, where again $t_{\mathrm{nor}} = \nu t/h^2$ is the time normalised with the cubes's height and fluid viscosity, which corresponds to $10t_{\mathrm{ft}}$.

2.2. Initial and boundary conditions

The inflow conditions at the entrance into the cross-flow channel and the top plenum chamber were generated from LES of a channel flow which was run simultaneously with the computation of the flow considered (Ničeno, 2001). In order to achieve a well defined, reproducible reference situation, the imposed flow quantities correspond to the isothermal ($\Theta_{\mathrm{in}} = 20$ °C) fully turbulent channel flow with the appropriate Reynolds number, although Tummers et al. (2005) stressed that in the experiment, the channel flow was not fully developed. The flow that was providing the inflow for the cross-flow channel had the Reynolds number defined by the channel height H and the channel bulk velocity U_{c}, while the Reynolds number of the flow that was providing the inflow for the plenum chamber was based on the chamber height $4D$ and the top chamber bulk velocity U_{top} that gives the wanted bulk velocity of the jet U_{j}.

At the downstream boundary, zero gradients have been imposed for all variables. No-slip boundary condition was used for the velocity at all walls, including the side walls in the main channel at $z/h = \pm 3.5$ and $4D \times 4D \times 4D$ in the top chamber. The constant temperature $\Theta_{\mathrm{in}} = 20$ °C was imposed at all walls, including the part of the wall in the base region of the cube where the epoxy layer is attached to the bottom wall. The only exception is the outer surface of the central cube $C3$: its temperature Θ_{w} was computed, simultaneously with the flow field, from the temperature evolution in the 1.5 mm thick low-conducting epoxy layer, given the temperature of the 13.5^3 mm^3 cube copper core $\Theta_{\mathrm{Cu}} = 70$ °C.

In the experiment, the bulk inflow information was extracted from the mass flow rate, and checked from the velocity measurements. The channel flow was developed after a $4.67h$ long honeycombed section placed 26 h upstream of the first cube $C1$, with a mass flux $\dot{m}_{\mathrm{c}} = 2.5 \times 10^{-2}$ kg/s. The jet is issued from an orifice that connects the channel containing the wall-mounted cubes and the 10 h long plenum chamber, with the mass flow rate $\dot{m}_{\mathrm{j}} = 8.5 \times 10^{-4}$ kg/s.

In the simulations, the most problematic was the specification of the jet inflow conditions that could reproduce accurately the experimental situation. Several authors (Muppidi and Mahesh, 2005; Kelso et al., 1996; Geers, 2004) emphasized how important it is to have accurate information about the flow in the jet exit plane. Unfortunately, in the present case the available experimental results appeared not to be sufficiently informative to reconstruct exactly the inflow of the jet into the cross-flow. The logical solution, therefore, was the inclusion of the jet plenum chamber into the computational domain so that the entire experimental geometry is simulated. Not only that in this way the geometry is realistically represented, but also the strong interaction between the jet at the exit of the orifice and the lateral flow, could be accounted for. Of course, the simulation of the flow in the plenum chamber allows these interactions to develop naturally.

Although highly preferable from numerical stability and accuracy point of view, obviously the periodic boundary conditions could not be applied, because only one of five – the central cube was heated and impinged by a jet. In order to speed-up the computation, the data from computations of the same configuration and with the same boundary conditions, but obtained with RANS model ζ–f which was proposed by Hanjalić and Popovac in 2004, were used to generate the initial velocity field.

2.3. Computational mesh

In order to resolve the intricate interactions especially in the near-wall and shear layer regions and to capture complex flow structures, special attention was paid to the optimization of the computational mesh aimed at minimizing the number of cells while still having sufficient mesh resolution around $C3$ cube. In the adopted meshing strategy, illustrated in Fig. 2, for each of the cubes and for the plenum chamber, a separate subdomain was designed, so that different flow regions can be adequately meshed. In the end, the total time spent on the generation of the mesh, including the development and the analysis of different meshing options, was nearly the same as the time spent on the effective simulations.

Based on the Kolmogorov scales estimation obtained from the separate RANS computations, the final LES mesh was generated with the total of 8.5×10^6 cells. The mesh around the $C3$ cube consists of several elements. In the circular part of the domain inside the jet an H-topology is used (quadratic prism is placed in the centre of the cylinder), followed by a hexagonal zone around the jet. This extends into a block of regular cubes in the streamwise direction up to $1h$ from the cube. By clustering the mesh towards the edges of the cubes, a finer resolution in the critical near-wall region has been achieved. In order to reduce the total number of cells, the mesh is "paved" with somewhat larger cells further away in the streamwise direction, but with a layer of fine cells clustered near the side boundaries. The same "paving" method was used to connect the cube subdomains with different spacing in the direction along the channel height. This meshing strategy allowed to have hexahedral cells in thin layers next to all boundaries, which improves numerical accuracy and stability of the computation. The mesh in the solid part of the domain (epoxy) consists of five layers of cells extruded from the mesh on the surface of the cube.

An illustration of the mesh quality and the LES constraints is given in Fig. 3, which shows the distribution of

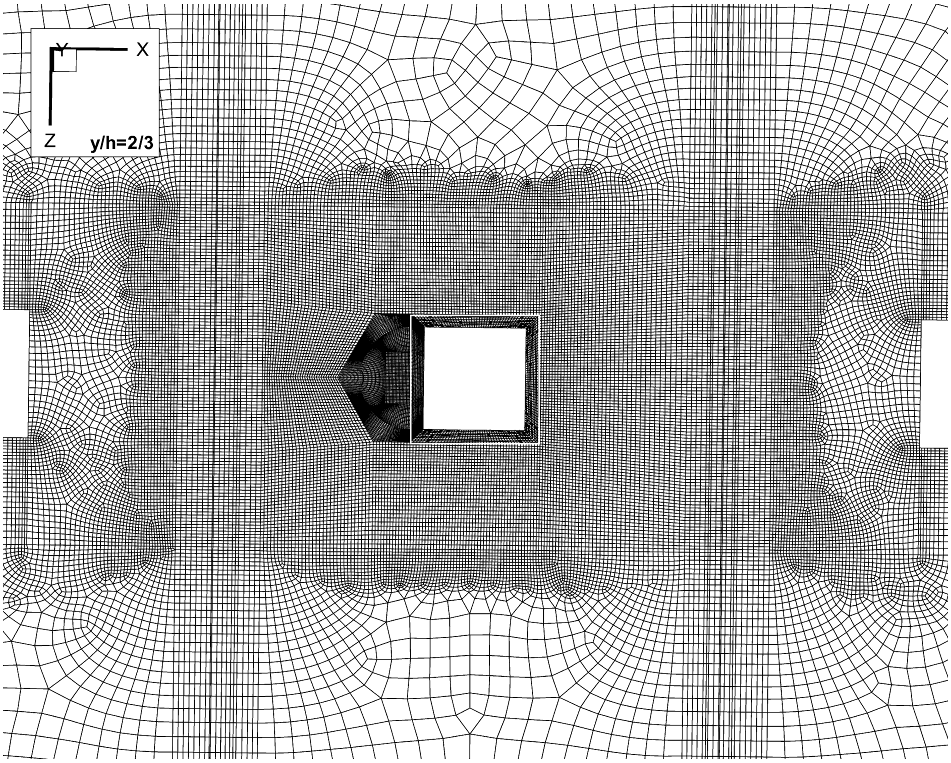

Fig. 2. Mesh organisation presented in a horizontal cutplane.

the cell spacings in different directions compared to the Kolmogorov length scale obtained from the separate RANS computation, as well as the grid spacing expressed in the wall units. In the region of most interest, i.e. approximately 1*h* around the central cube, the grid spacing follows well the recommendations with respect to the local Kolmogorov scale $\mathcal{O}(\Delta x^+) = \mathcal{O}(\Delta y^+) = \mathcal{O}(\Delta z^+) = 10L_{\mathrm{Kol}}$.

Another check for the mesh quality in LES is the *a posteriori* analysis of the level of the modelled subgrid-scale turbulent viscosity. A good indicator of this level is the time series of the ratio between the computed eddy viscosity and the molecular viscosity, taken at several characteristic monitoring locations. It is clear from the time variation of this ratio, given in Fig. 4, that closer to the wall the

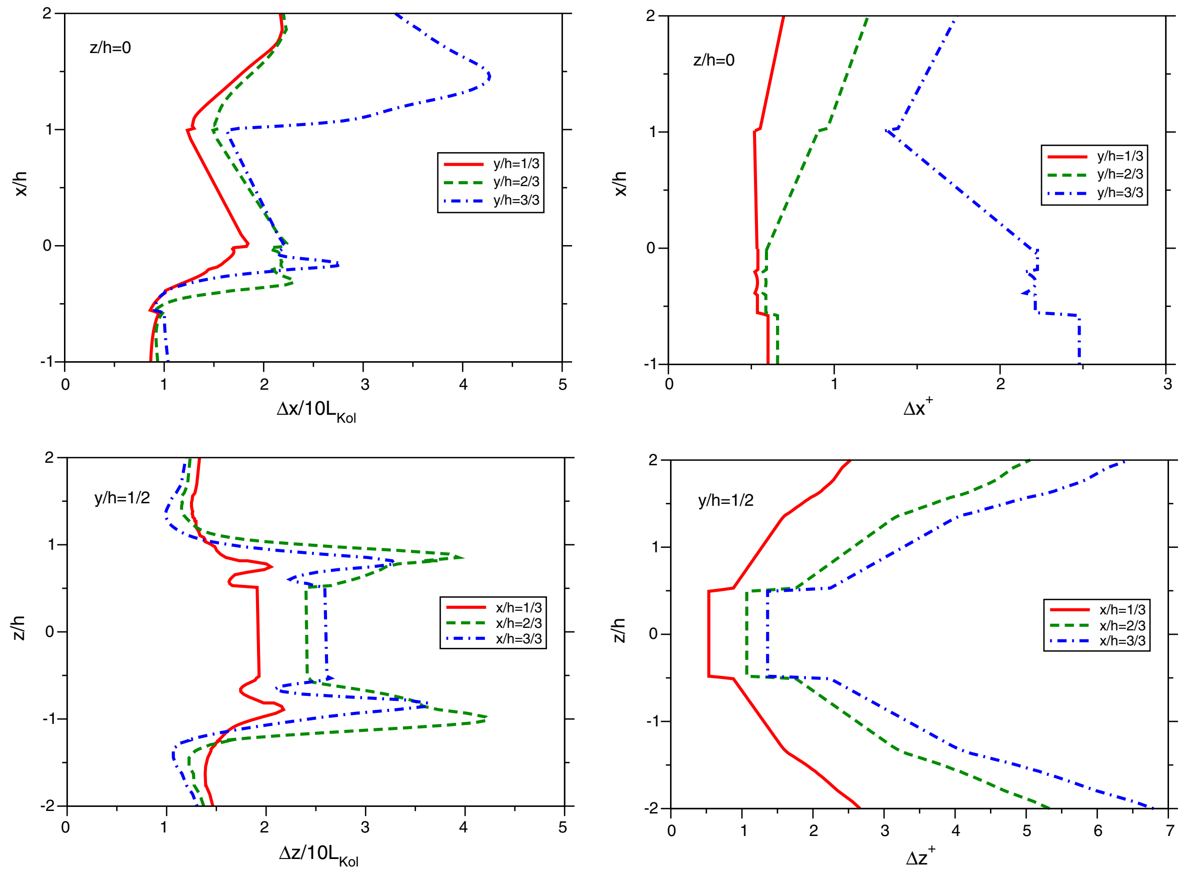

Fig. 3. Distribution of the cell spacing for the LES mesh at different locations in *x*-direction (top) and *z*-direction (bottom): comparison with the Kolmogorov scales (left) and in wall units (right).

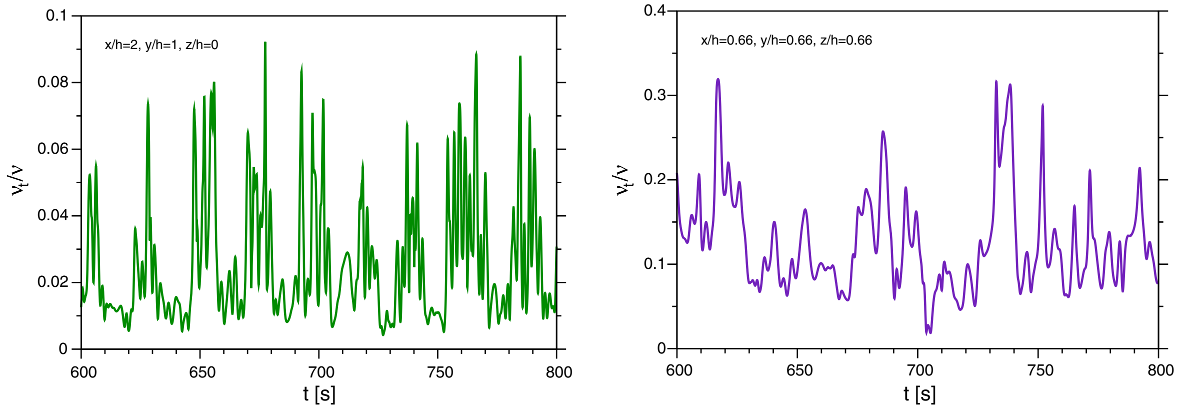

Fig. 4. Ratio of the eddy viscosity to molecular viscosity at the characteristic monitoring points: in the wake of the cube (left), and on the side of the cube (right).

modelled part is somewhat higher than in the farfield region, yet the obtained values are around the recommended value of $\nu_t/\nu \approx 10\%$.

3. Results and discussion

The overall flow pattern observed in the experiment by Tummers et al. (2005) has been well reproduced in the LES solution, as illustrated in Fig. 5. The major feature is the jet splitting into a part that impinges on the top cube surface, and the part that sweeps along the cube front face and eventually impinges on the channel bottom wall in front of the cube. What follows is a complex interaction of the split jet and the channel cross-flow over and a round the cube. However, a quantitative comparison of flow parameters in some flow regions reveals some differences between the measured and simulated results. These differences are due to the earlier mentioned mismatching of the experimental and simulated jet-orifice axis with respect to the central cube leading edge. Due to this small shift of $(S' - S)/h = 0.03$, approximately 10% more of the jet momentum passes along the front face of the central cube in the experiment as compared to LES, and vice versa – in the simulation approximately 10% more of the jet momentum is impinging onto the central cube as compared to the experiment. This geometrical discrepancy is reflected in the results, as discussed below.

3.1. Flow pattern and vortical structures

A major feature of a jet in a cross-flow is the jet deflection (see Fig. 5), caused by the pressure exerted on the jet by the lateral flow. The intensity of the deflection depends on the geometry and the velocity ratio α_v, which governs the mixing of the two streams in the jet periphery. Due to the collision of the two mutually perpendicular streams and the entrainment process, which is a shear-driven interaction between the jet and the lateral cross-flow, the jet begins to acquire a characteristic kidney shape. In the present case the deflection is intensified by the decrease of the jet's cross-section due to the convergence of the streamlines, caused by the sharp-edge shape of the jet orifice. This is the well known *vena contracta* effect, readily seen in Fig. 6.

In the given setup the jet is formed by fluid issuing from the top chamber through a round orifice in its bottom wall. The streamwise momentum of the chamber fluid is partly carried over by the fluid entering the orifice and generating some tangential motion. This, together with the lateral flow bends the jet in the streamwise direction already within the orifice resulting in an nonsymmetric velocity distribution

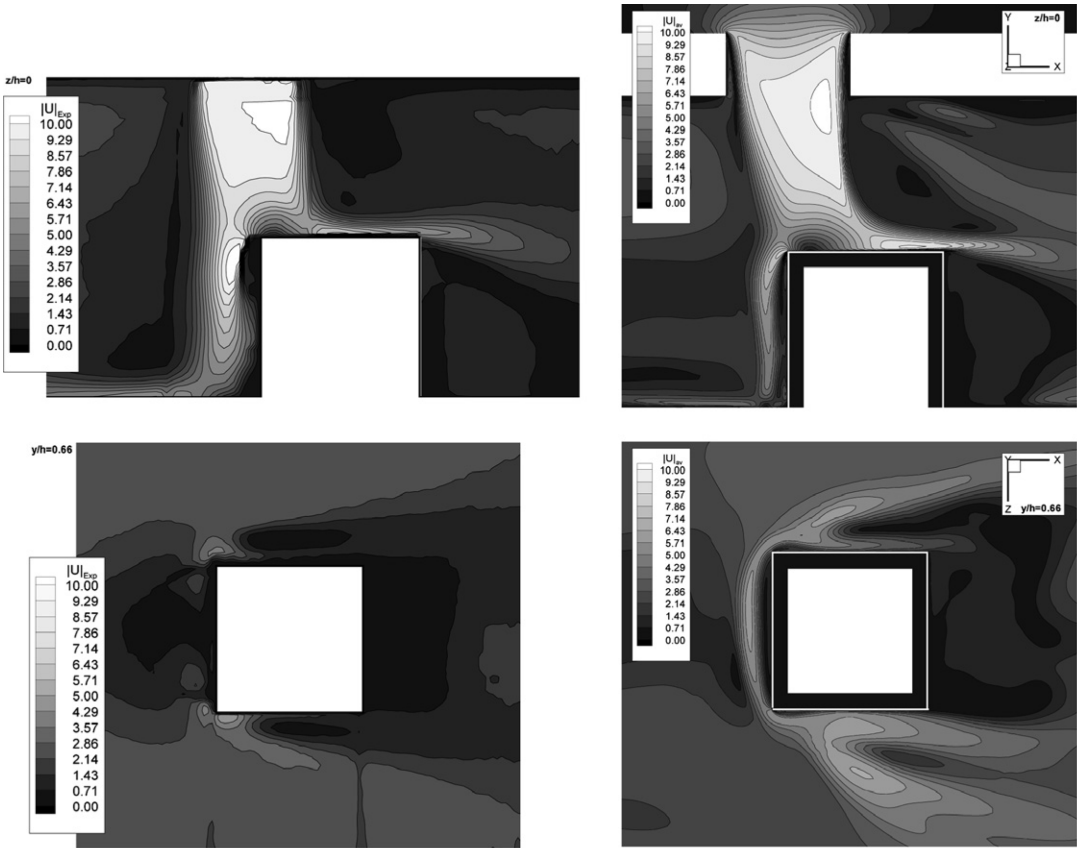

Fig. 5. Contour plots of the average velocity magnitude from the experiments (left) and LES (right) in the vertical midplane $z/h = 0$ (top) and the horizontal cutplane $y/h = 0.66$ (bottom).

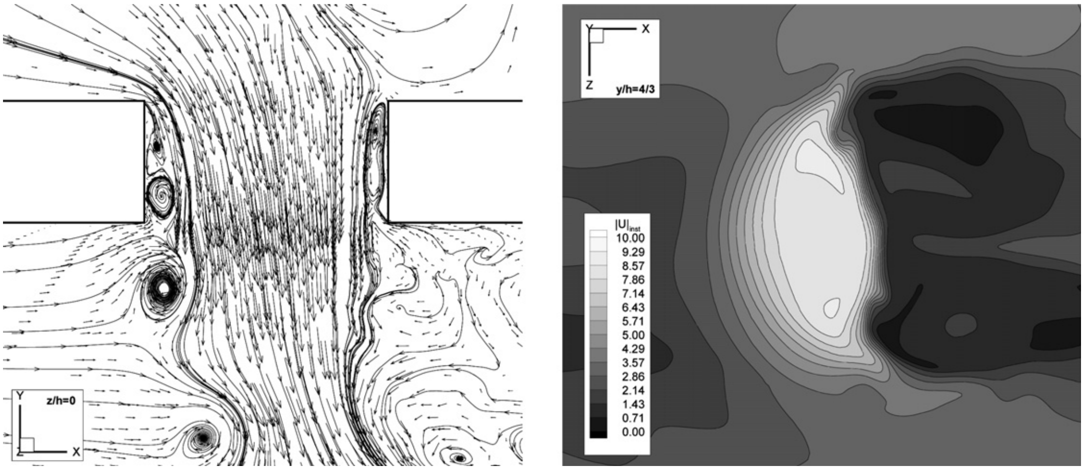

Fig. 6. Instantaneous pathlines and the velocity vectors in the vertical midplane $z/h = 0$ showing the *vena contracta* effect, the entrainment in the jet shear layer and the formation of the vortex rings (left), and the contour plot of the instantaneous velocity magnitude showing the deformation of the jet shape 2/3*h* below the orifice exit (right).

with its peak shifted from the orifice centre to a location to the right – in the direction of the chamber – and channel flow. Moreover, the shear induced by the lateral flow will generate some circumferential motion at the jet periphery. Apparently this tangential motion is neither steady nor symmetric, what results in the rotation of the fluid in the orifice in one or other direction. This creates an instantaneous swirling, especially in the jet core, which extends along the core of the jet all the way to the top face of the central cube. Since the computational setup was fully symmetric along the central vertical plane, the established direction of the swirl is just one of the possible two solutions, depending on the initial flow disturbance. In a real situation, this disturbance can originate from various imperfections in the flow, whereas in numerical simulations it can be triggered by a numerical bias in solving the discretized equations, (i.e. the adopted sweep direction, sequence in which equations are solved etc.). Once the swirl is established, it seems that it keeps a prevalent direction, as indicated by time-averaged plots, although instantaneous solutions may have opposite rotation. From the pathlines (not shown here) it is clear that the swirling is intensive only within the central region of the jet (the core).

When the fluid from the top chamber flows into the orifice over its upper (sharp) edge at the chamber's bottom wall, a separation region is created within the orifice. Shear instabilities of the Kelvin–Helmholtz type develop in the shear layer separating the bubble and the rest of the jet. On the other hand, as clearly seen in Fig. 6, the channel cross-flow hits the jet and a part of the channel fluid enters into the orifice creating another, stronger recirculating bubble in the lower part of the orifice just above the channel upper wall. A strong horseshoe vortex develops around the upper part of the jet entering the channel flow and a similar counter-rotating one further downstream the jet just above the cube.

These two horseshoe vortices are in fact the two conspicuous examples of remnants of the periodic roll-up vortex rings that develop in the shear layer of any free jet, deformed and convected downstream by the lateral channel flow. They are characterised by the local low pressure, and can clearly be identified in Fig. 7, which shows a time sequence of the instantaneous pressure isosurfaces coloured by the instantaneous velocity magnitude. As these large scale structures are very strong, they have a significant influence on the mixing process and the cooling of

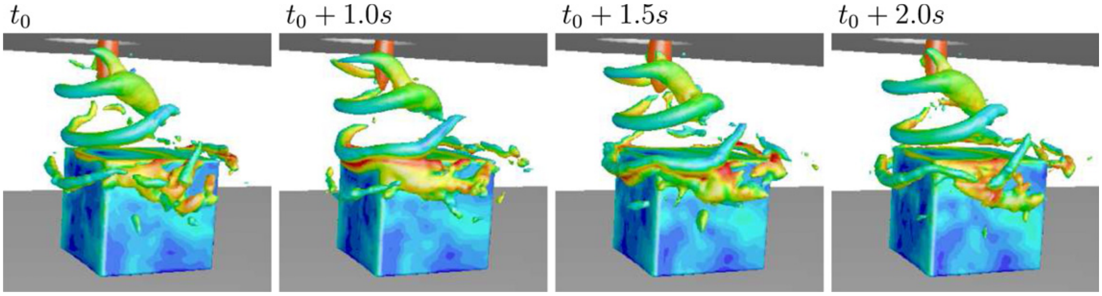

Fig. 7. Creation and behaviour of vortex rings, visualised by the instantaneous pressure isosurface coloured with the instantaneous velocity magnitude, given by the time series of the instantaneous flow snapshots.

the cube. Initially some of these structures keep the ring shape and stay parallel to the orifice edge, but as they travel along with the jet they are bending following jet's deflection and breaking into typical horseshoe shape.

On the downwind side of the jet the rings are breaking up faster, while the upwind ones retain their identity and disperse only after hitting the surface of the cube. The characteristic frequency of these vortex rings corresponds to $St = 0.81$, where the Struohal number is based on the orifice diameter D and the jet bulk velocity U_j. The obtained value of the Strouhal number falls within the range reported by UCLA group (Shapiro et al., 2006), who investigated a jet in a cross-flow at various velocity ratios α_v.

The downwind and the centreline jet streamlines impinge onto the central cube, while the upwind part of the jet passes in front of the cube and impinges onto the bottom wall of the channel.

After impinging onto the channel bottom wall, the upwind part of the jet splits in two parts: the one that creates the corner vortex at the bottom of the front face of the central cube, and the other that is merging with the bottom horseshoe vortex in front of the central cube. The central and downstream jet streamlines, which impinge onto the central cube, deflect on the top face, move towards all the edges of the face and separate there. At the leading edge, the streamlines deflect the lateral flow and create a separation bubble on the upper part of the cube front face. At the trailing edge these streamlines indicate massive separation of the lateral bulk flow that takes place behind the cube and creates the arch vortex. At the front corner of the side edges the side edge vortices are created. Also, prior to the orifice, another horseshoe vortex attached to the upper channel wall is formed around the jet at the orifice exit, with a recirculation bubble created behind the jet.

This brief overview of the flow pattern and vortical structure covers only the most conspicuous and well identifiable vortices, and serves as a basis for interpreting the mean flow and turbulence statistics profiles, discussed below.

3.2. Mean flow and turbulence statistics

A detailed overview of the mean velocity and turbulence second moments has been reported elsewhere (Popovac, 2006), and we present here a selection of results to illustrate the qualitative and quantitative comparison with the experiments, and to point out at some major flow features and turbulence dynamics, especially those relevant to heat transfer. The comparison illustrates also how difficult it is to mimic an experimental setup when dealing with a complex flow.

As stated above, the contour plots of the mean velocity magnitude in the vertical and horizontal cutplanes illustrate the overall agreement of the LES results with the experiment, Fig. 5. While the general flow pattern obtained by LES is in a satisfactory agreement with the experiments, one can observe that the flow contours are not symmetric. This is the consequence of insufficient averaging time, but as the inflow conditions are symmetric the contour plots in the horizontal cutplanes will be shown only for the half of the plane, assuming the symmetry.

The comparison of the contours of the resolved part of the streamwise $\overline{uu}$ and the vertical $\overline{vv}$ turbulent normal stress components and of the associated turbulent shear stress $\overline{uv}$, presented in Fig. 8, shows also reasonable agreement. For illustration, Fig. 9 shows the contours of the resolved part of other two shear stress components ($\overline{uw}$ and $\overline{vw}$) in two cutplanes, but no comparison with experiments can be made here since no experimental data for these components in the considered planes are available.

Further quantitative comparison between the experimental data and LES results is presented in Figs. 10–13, which show selected profiles of the mean velocity components and of the resolved part of the streamwise turbulent stress. The profiles in the y-direction of the velocity modulus in the vertical midplane $z/h = 0$ are shown in Fig. 10, and the profiles of the streamwise velocity component in the horizontal cutplane $y/h = 0.66$ are given in Fig. 11 for the z-direction. For the comparison of the turbulent quantities, the profiles of $\overline{uu}$ normal component of the resolved part of the turbulent stress in the horizontal cutplane $y/h = 0.66$ are presented: in Fig. 12 the cutlines are in the x-direction, and in Fig. 13 the cutlines are in the z-direction. Another quantitative comparison between LES results and the experimental data is given in Table 3, which lists the locations of the most important parameters pertinent to elements of the flow structures occurring in the flow.

While at some cutplanes the LES results agree very well with the experiments, some plots show noticeable difference. Namely, as said above, the bending of the jet is stronger in the LES than in the experiments, and the location of the horseshoe vortex in front of the cube and the position of the local maxima in some profiles is shifted (e.g. in Fig. 10 for the profiles $x/h = \pm 0.33$, or in Fig. 13 for the profile $x/h = 0.33$). These all come from the difference in the distribution of the jet momentum between the experiments and LES, or in the case of the top part of the velocity profiles at $x/h = \pm 0.33$ in Fig. 10 simply due to the geometrical shift in the position of the orifice.

The differences noticeable in the above figure and the table originate from the small differences between the experimental and numerical setup, discussed above. The main source of discrepancy is the seemingly marginal, but apparently influential difference in the positioning of the jet centre relative to the cube. This small difference of 0.5 mm was initially regarded as unimportant, but the LES studies of the effect of inflow conditions revealed that the flow is very sensitive to even small changes in the flow configuration. The other reason for difference between the LES and experimental results are associated with the inability to mimic in full the inflow conditions, simply because of the lack of detailed experimental data. In order to minimize the effect and to reproduce closely the flow and turbulence conditions in the jet, LES has been conducted for the

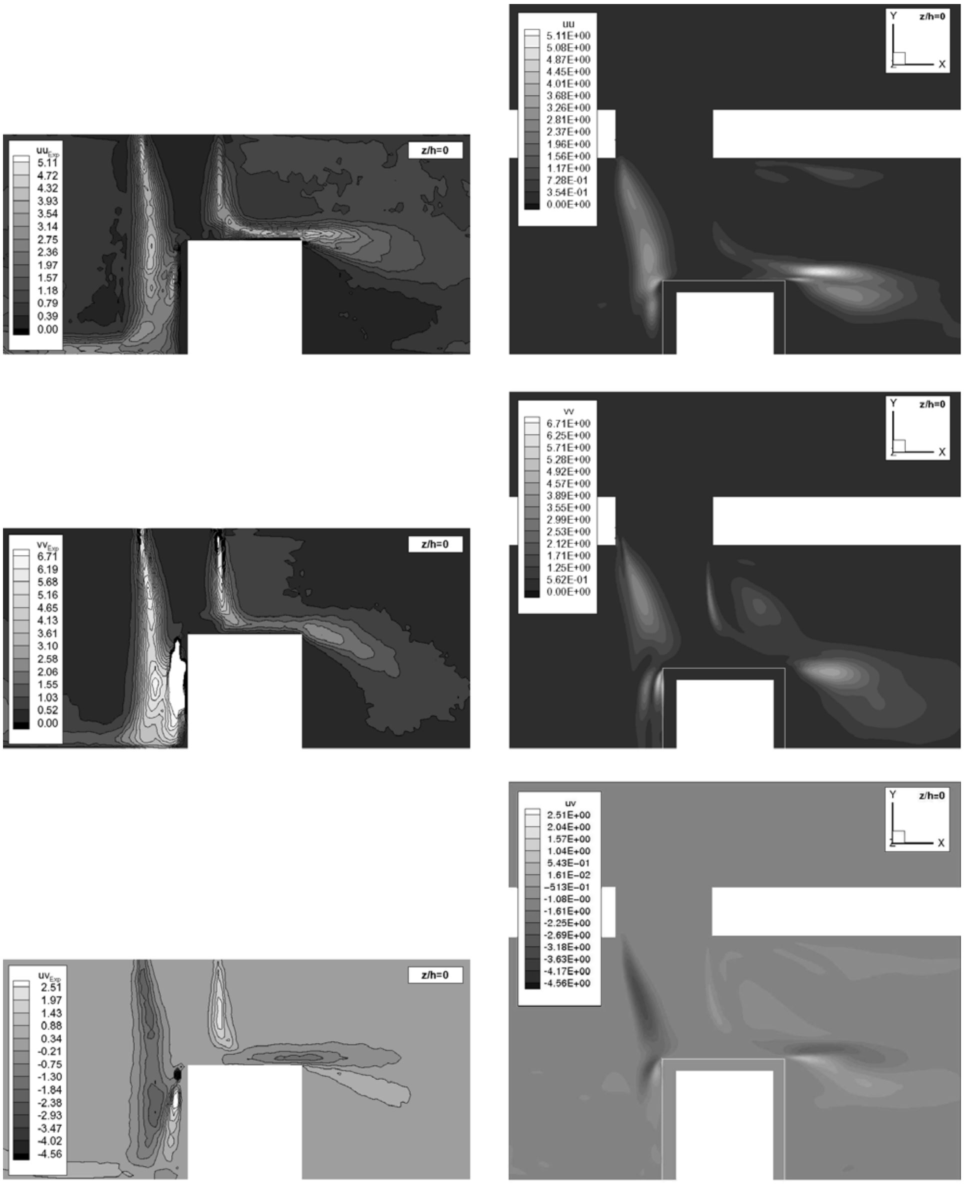

Fig. 8. Contour plots of the turbulent stresses $\overline{uu}$, $\overline{vv}$ and $\overline{uv}$ (from top to bottom) in the vertical midplane $z/h = 0$, obtained from the experiments (left) and LES (right).

chamber flow in parallel, but the uncertainty in the entry flow into the chamber remained. For these reasons, the LES here presented and the experiments cannot be directly compared for the sake of validation, but should be regarded each on its own merit.

3.3. Turbulent stresses and their budgets

The contours of selected turbulent stress components (only their resolved part is presented in this article) shown in Figs. 8 and 9 indicate the zones of high turbulence intensity, which is characterized by high values of all normal turbulent stresses. These zones are found primarily in jet edge shear layer and regions of interaction with the cross-flow and entrainment of the lateral flow into the jet. High turbulence intensity is observed also in the region of the flow bending over the edges of the cube and in the wake behind the cube and the jet. The distribution of the wall-normal and the streamwise components of the normal turbulent stresses $\overline{uu}$ and $\overline{vv}$ depicts certain qualitative and quantitative similarities, with their respective local maxima in the shear layer of the jet and around the cube. The spanwise normal turbulent stress $\overline{ww}$ behaves differently: its maxima are in the wake of the jet, in the recirculation zone behind the cube and in the horseshoe vortex in front of the cube.

Unlike the normal stresses, $\overline{uv}$, $\overline{uw}$ and $\overline{vw}$ have their respective maxima not in the vertical midplane $z/h = 0$ but on the side planes of the cube. Aside from the shear layer on the trailing edge of the top face of the cube, the most intense shearing occurs on its front corner where the edge vortex EV is created. The shape of the region with increased level of the shear turbulent stresses follows the

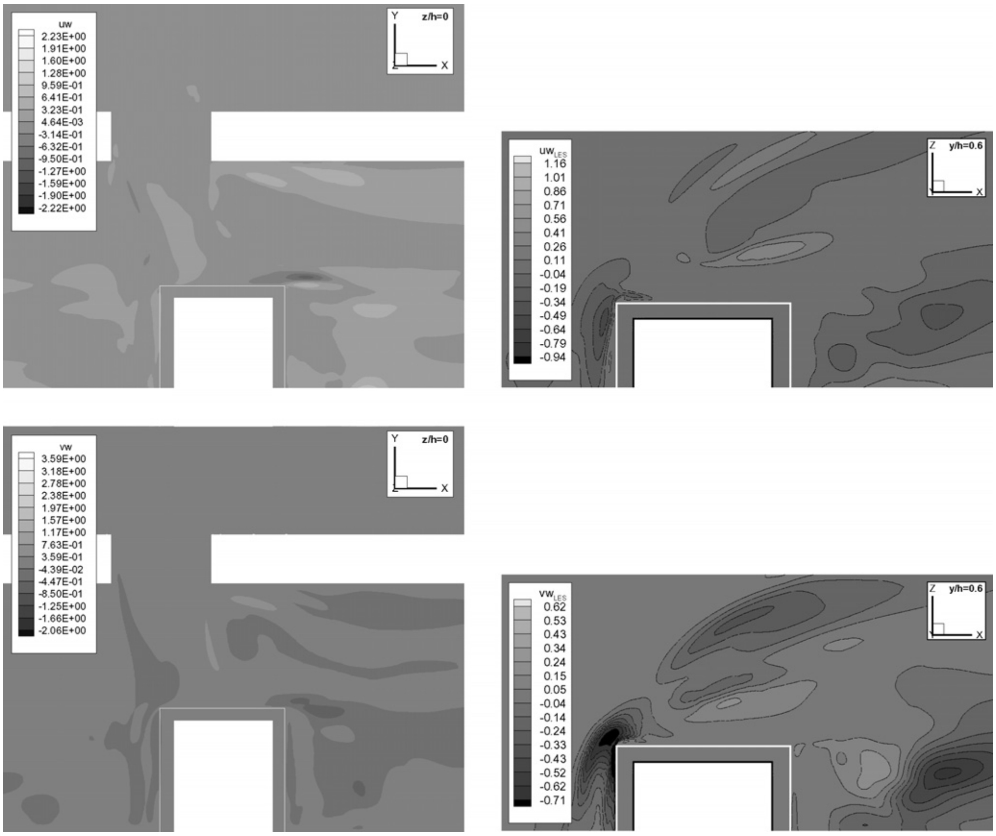

Fig. 9. Contour plots of the shear components of the Reynolds stress tensor $\overline{uw}$ (top) and $\overline{vw}$ (bottom) in the vertical midplane $z/h = 0$ (left) and the horizontal cutplane $y/h = 0.66$ (right), obtained from LES.

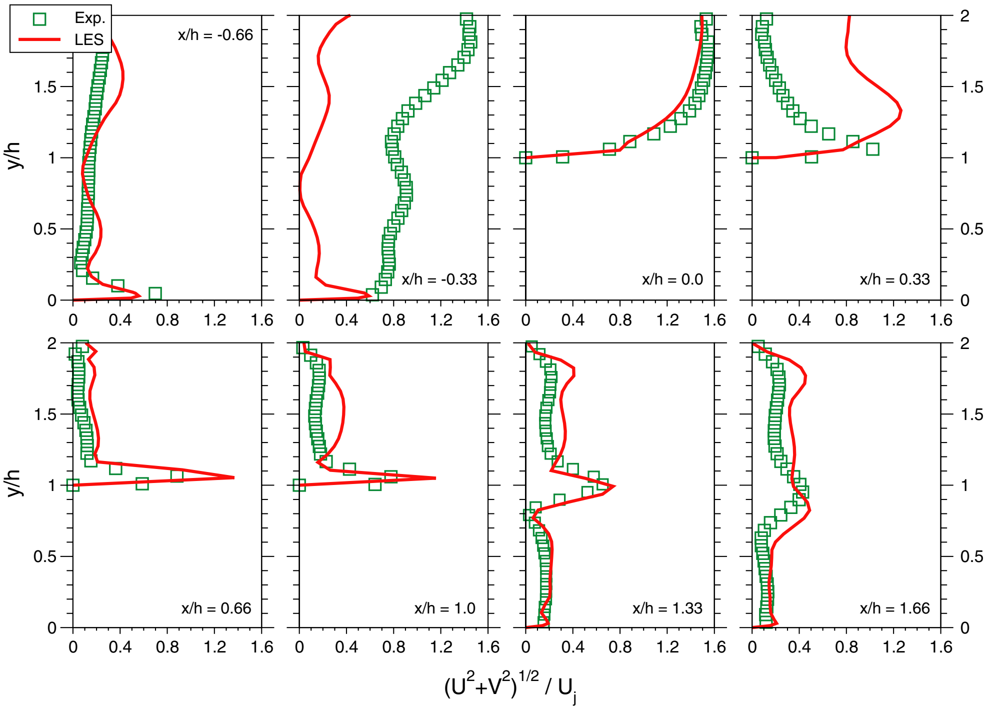

Fig. 10. Profiles of the $(U^2 + V^2)^{1/2}$ velocity intensity in the wall-normal direction in the vertical midplane $z/h = 0$, obtained from the experiments and LES.

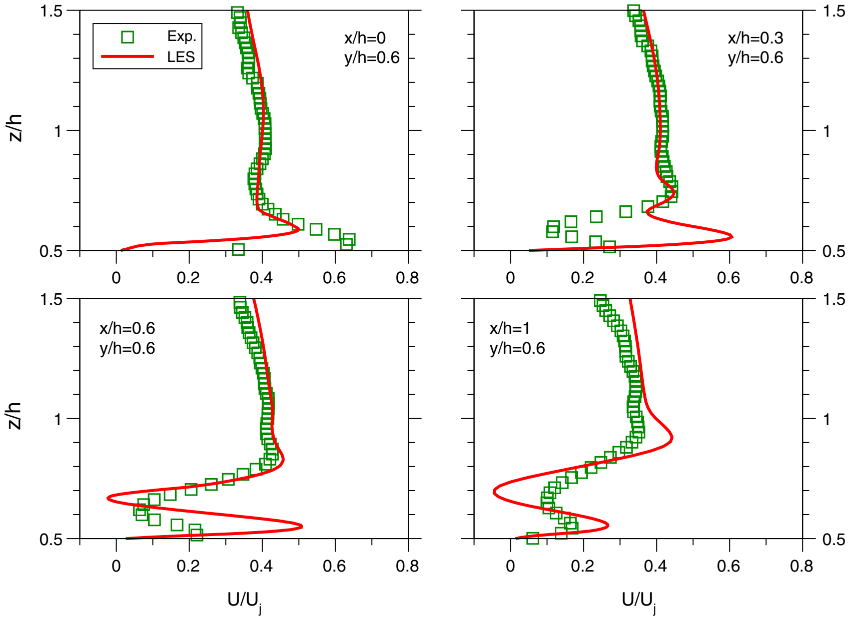

Fig. 11. Profiles of the U velocity component in the spanwise direction in the horizontal cutplane $y/h = 0.66$, obtained from the experiments and LES.

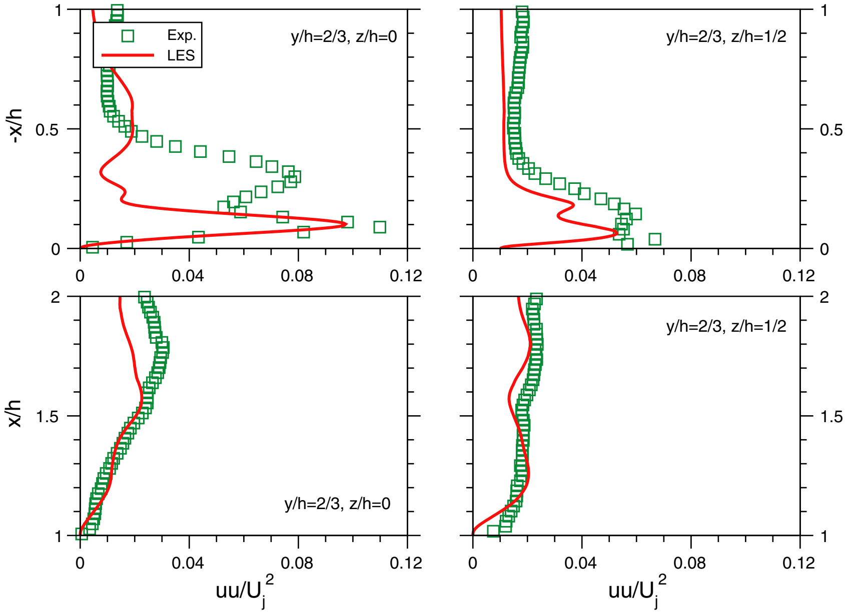

Fig. 12. Profiles of the $\overline{uu}$ normal turbulent stress component in the streamwise direction in the horizontal cutplane $y/h = 0.66$, obtained from the experiments and LES.

shape of this vortex: starting from the upper front corner of the side face and spreading in the diagonal direction along that face.

In order to depict the mechanism of the energy transport around the cube, the budgets of all turbulent stress components have been evaluated. Fig. 14, showing contours of all constituents of the $\overline{uu}$ budget, illustrates the dynamics of this stress component for the vertical midplane $z/h = 0$. To describe this mechanism, let us follow imagined pathlines that enter into the domain through the orifice. First, after encountering the cross-flow the turbulent stresses are generated in the shear region of the jet. There they are partially redistributed by means of the pressure–velocity scrambling, diffused and mainly advected by the jet towards the cube. When the jet impinges onto the top face of the cube the mean velocity tends to zero, hence the convection is negligible. The dominant effect for the energy transport in that region is represented by the velocity–pressure gradient term, while the production of the normal turbulent stresses gets negative.

After the impinging onto cube top face, the fluid that escapes from the impingement region flows over the leading

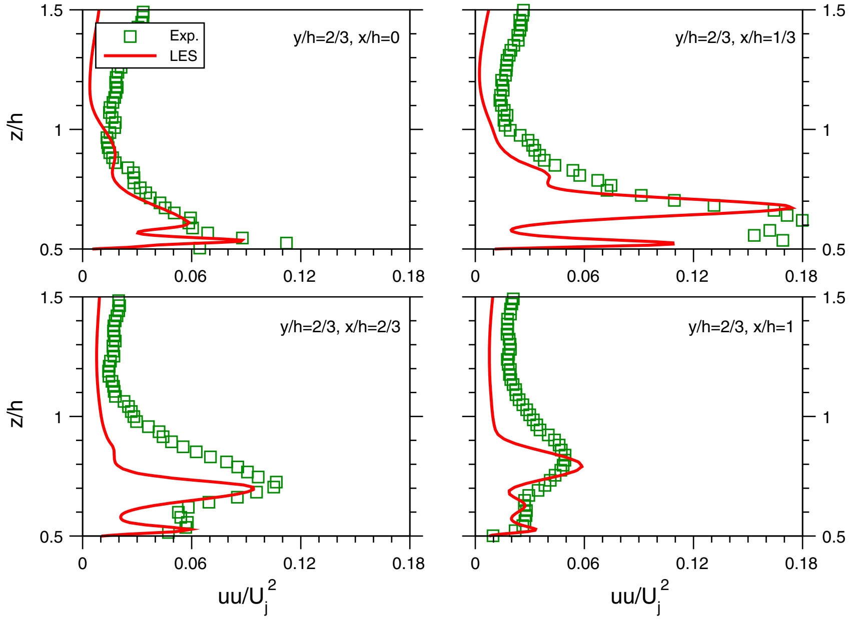

Fig. 13. Profiles of the $\overline{uu}$ normal turbulent stress component in the spanwise direction in the horizontal cutplane $y/h = 0.66$, obtained from the experiments and LES.

Table 3
Position of the dominant flow structures in the vertical midplane $z/h = 0$

	LES		Experiment	
	x/h	y/h	x/h	y/h
Coordinates of the impinging point on top face	0.15	1.00	0.10	1.00
Coordinates of the impinging point on mounting wall	−0.15	0.00	−0.29	0.0
Length of the corner eddy	0.00	0.23	0.0	0.29
Height and depth of the separation bubble	0.00	0.39	0.00	0.20
Centre of the bottom horseshoe vortex	−1.18	0.27	−1.50	0.40
Centre of the arch vortex	1.49	0.81	1.30	0.80

edge of the cube, where it undergoes very strong shearing. This implies a high production of the turbulent stresses, which is counterbalanced by the turbulent pressure and velocity diffusion. There is a region of high turbulent shear stress level on the trailing edge of the top face of the cube, hence the same scenario happens in that region as well. Only very close to the solid boundary along all the faces of the cube the viscous diffusion and the dissipation are making the balance in the energy budget.

On the side face of the cube the side-edge vortex is the dominant flow structure, hence the energy transfer mechanism is related to the behaviour of this structure. The production of the normal turbulent stresses remains negative in the region along the entire leading edge of the cube. Therefore, the dominant term in this region is again the velocity–pressure gradient correlation. Unlike in the impingement zone, at the side corner of the cube the convection is rather strong, as well as the turbulent diffusion. The influence of the viscous diffusion and the dissipation is again limited to the region very close to the wall.

Under the stabilising flow conditions the energy of turbulence can flow back into the mean motion. This reverse energy transfer, possibly accompanied with the reverse energy cascade in the spectral space (backscatter) can occur only locally and usually in the regions of high flow anisotropy. It has been confirmed both experimentally (Geers, 2004) and numerically (Hadžiabdić, 2006) that the production of the turbulent kinetic energy becomes negative in impinging jets in the region around the impingement centre. In the present case there are two impingement zones: on the top face of the cube and on the bottom wall just in front of the cube, and in both regions the production of k is negative.

For a quantitative view on the budgets of the turbulent stresses, Figs. 15–17 give respectively the profiles of the $\overline{uu}$, $\overline{vv}$ and $\overline{ww}$ stresses in the cutlines above the top face of $C3$ cube in the y-direction. The energy transfer in front and behind the central cube is given quantitatively by the profiles of the $\overline{uv}$ and $\overline{uw}$ stress budgets in the x-direction, as presented in Fig. 18.

In the impingement region the most important is the velocity–pressure gradient correlation, which is counterbalanced by the negative production. In the shear layer of the jet and in the recirculation region behind it there is strong production of the turbulent stresses. Due to the deflection of the jet, the convection term is always present near the top face of the cube $C3$. Convective transport is very intensive also in the region behind the jet. The viscous diffusion and the dissipation term are generally very small, except for very close to the surface of the cube.

In the bottom horseshoe vortex, which is the dominant flow structure in front of the cube $C3$, the most important energy transfer mechanism is the convection, which is

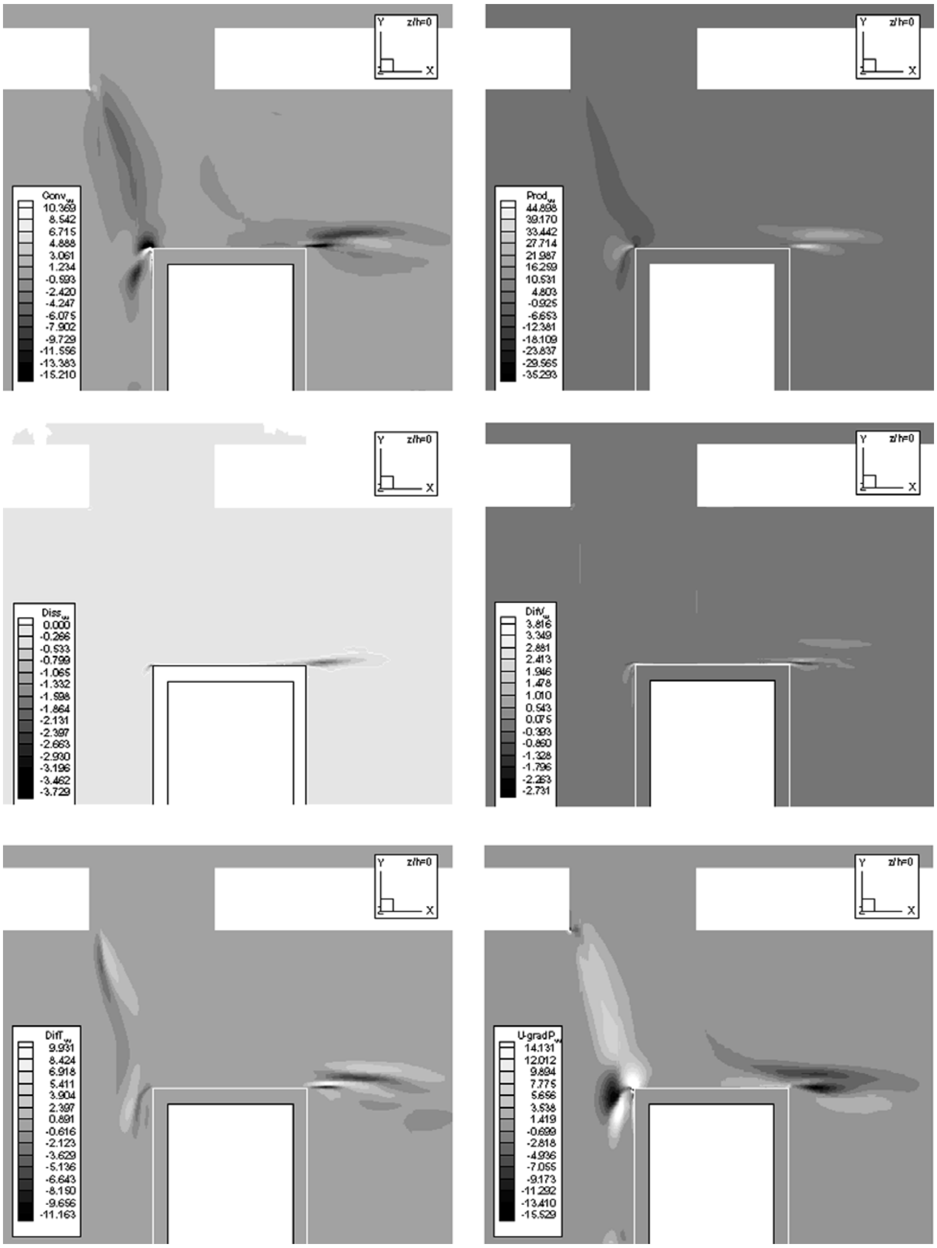

Fig. 14. Budget terms of the normal Reynolds stress component $\overline{uu}$, presented as the contour plots in the vertical midplane $z/h = 0$. From top to bottom: convection $\mathscr{C}_{uu}$, production $\mathscr{P}_{uu}$, dissipation ε_{uu}, viscous diffusion $\mathscr{D}^{\nu}_{uu}$, turbulent diffusion $\mathscr{D}^{t}_{uu}$ and velocity–pressure gradient correlation Π_{uu}.

counterbalanced by the production term and to some extent by the turbulent diffusion. The velocity–pressure gradient correlation term is generally very small in front of the central cube. The exception is the cutline closest to the bottom wall due to the influence of the second impingement point, and the cutline at the leading edge of the cube due to the influence of the first impingement point.

3.4. Temperature field

We move now to present some results of the temperature field computed in the epoxy layer in parallel with the LES. Because of very low conductivity, the temperature field in the epoxy layer does not change very fast and lacks behind the dynamics of the velocity field, but the cube surface nevertheless reflects the configuration of the dominant vortical structure close to the cube and their signature on the cube walls.

We begin by presenting the time-averaged temperature along the cutlines in the vertical and horizontal midplanes. Meinders (1998) concluded from his experimental investigation of the conjugate heat transfer from a single wall-mounted cube in a channel flow that the convective heat transfer coefficient does not depend on the value of the temperature imposed on the inner wall of the epoxy layer, hence implicitly on the level of the surface temperature. Therefore Fig. 19 gives the temperature difference between the temperature of the surface and the inflow temperature

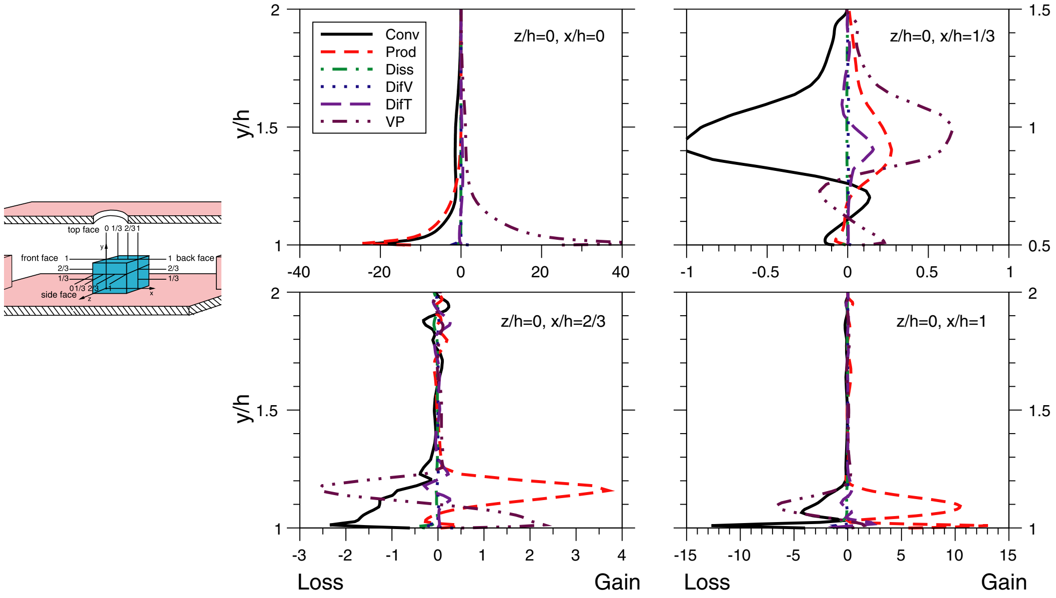

Fig. 15. Profiles of the $\overline{uu}$ budgets (convection $\mathscr{C}_{uu}$, production $\mathscr{P}_{uu}$, dissipation ε_{uu}, viscous diffusion $\mathscr{D}^{v}_{uu}$, turbulent diffusion $\mathscr{D}^{t}_{uu}$ and velocity–pressure gradient correlation Π_{uu}) above the top face of the cube $C3$ in the vertical midplane $z/h = 0$.

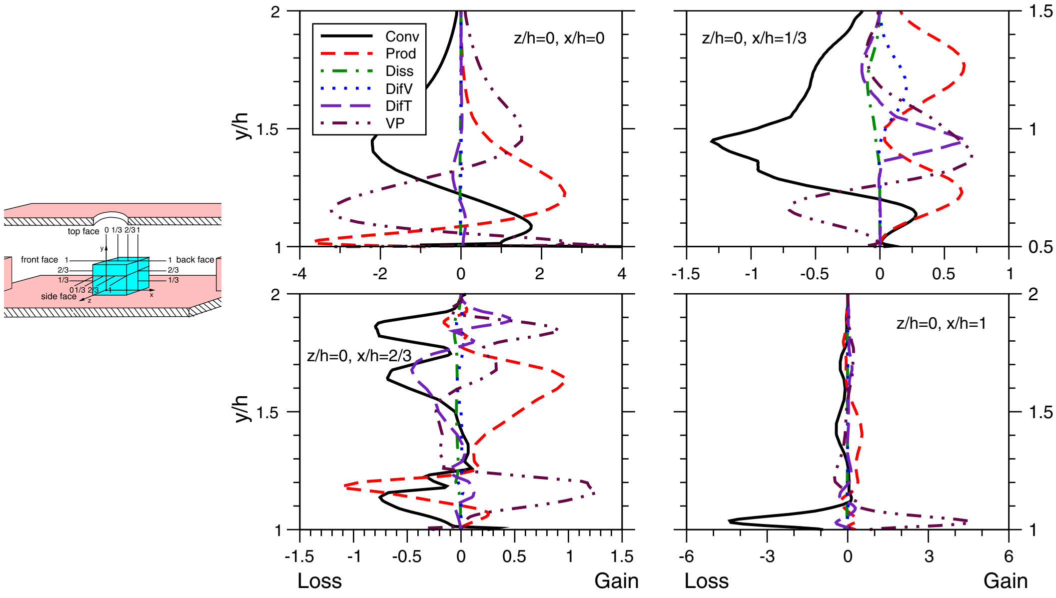

Fig. 16. Profiles of the $\overline{vv}$ budgets (convection $\mathscr{C}_{vv}$, production $\mathscr{P}_{vv}$, dissipation ε_{vv}, viscous diffusion $\mathscr{D}^{v}_{vv}$, turbulent diffusion $\mathscr{D}^{t}_{vv}$ and velocity–pressure gradient correlation Π_{vv}) above the top face of the cube $C3$ in the vertical midplane $z/h = 0$.

$\Delta\Theta = \Theta_{\mathrm{w}} - \Theta_{\mathrm{in}}$, normalised with the jet velocity U_{j} and the heat flux q_{w}: $\Delta\Theta_{\mathrm{nor}} = \Delta\Theta\rho c_p U_{\mathrm{j}}/q_{\mathrm{w}}$, where the heat flux is calculated from the conduction in the epoxy layer: $q_{\mathrm{w}} = \lambda_e(\Theta_{\mathrm{Cu}} - \Theta_{\mathrm{w}})/\delta$.

The most noticeable difference between the LES and experimental results occurs in the bottom part of the cube due to the difference in the treatment of the bottom wall–central cube junction, and the discrepancy around the edges of the cube is attributed to inadequate heat flux definition there. Based on the argument of the coupling between the velocity and the pressure field on one side, and the velocity and the temperature field on the other, Meinders (1998) also suggested that the averaged relative heat flux can be related to the averaged relative pressure. This qualitative relationship is presented in Fig. 20.

For the functionality of the electronic components the occurrence of *hot spots* is as dangerous as an excessive steady temperatures themselves. Hot spots are the isolated regions of high temperature, and they are causing high thermal stresses in the solid. The most critical is the rear face of the cube because of strong recirculation in the wake. Here, the fluid trapped into the recirculation gets heated,

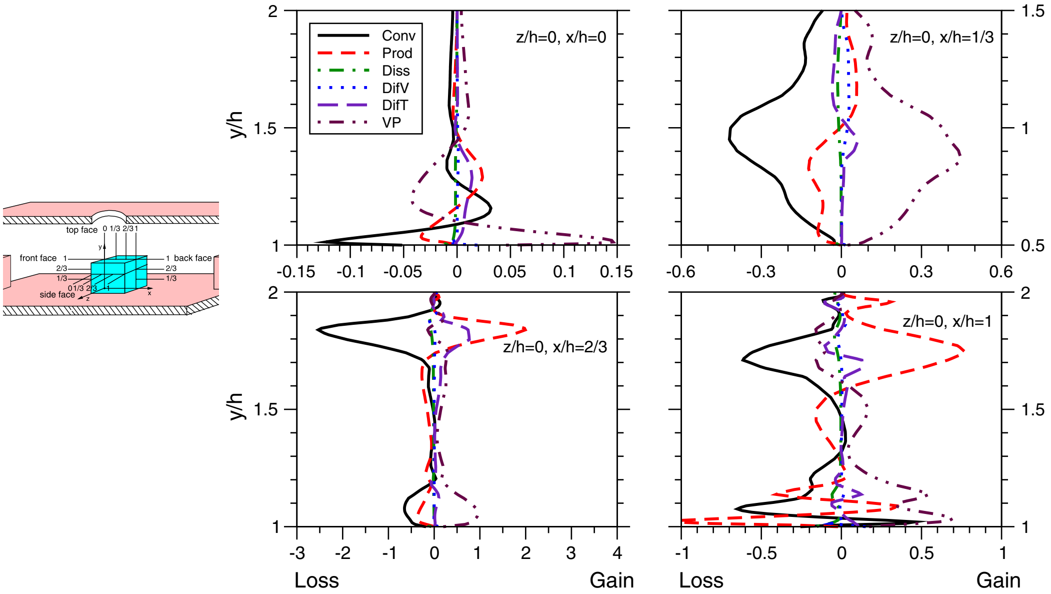

Fig. 17. Profiles of the $\overline{ww}$ budgets (convection $\mathscr{C}_{ww}$, production $\mathscr{P}_{ww}$, dissipation ε_{ww}, viscous diffusion $\mathscr{D}^{v}_{ww}$, turbulent diffusion $\mathscr{D}^{t}_{ww}$ and velocity–pressure gradient correlation Π_{ww}) above the top face of the cube $C3$ in the vertical midplane $z/h = 0$.

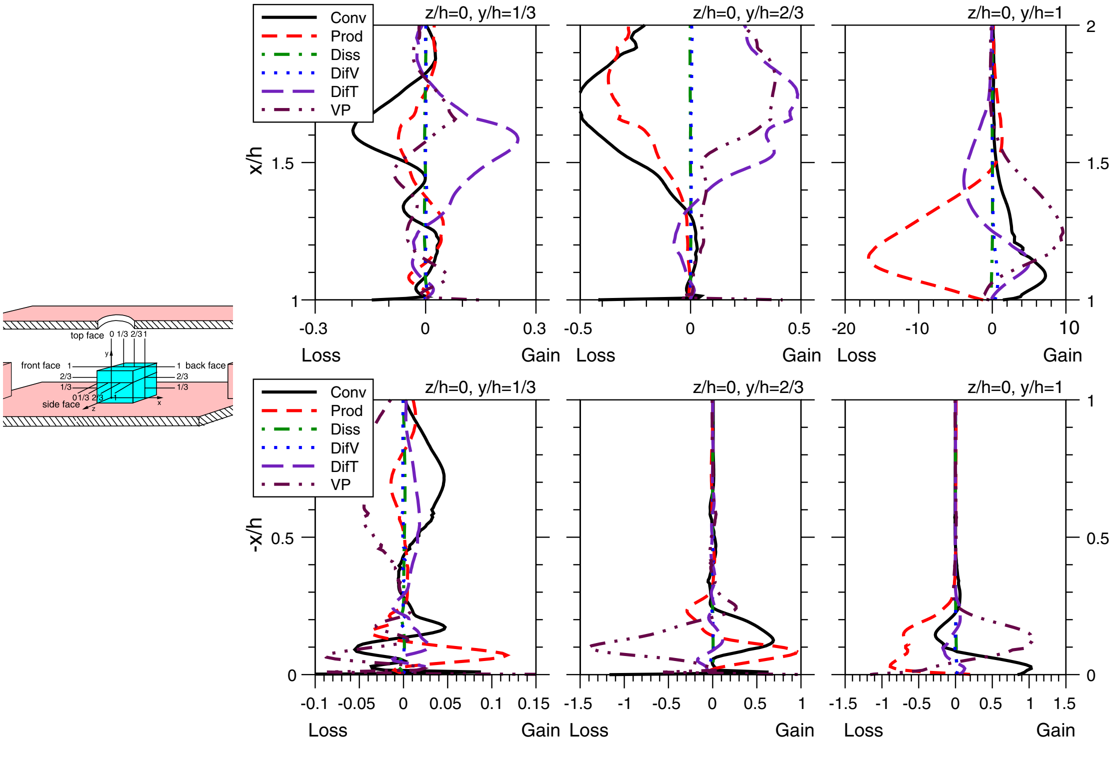

Fig. 18. Profiles the $\overline{uv}$ budgets in front of the front face of the cube $C3$ (top), and the $\overline{uw}$ budgets behind the back face of the cube $C3$ (bottom) in the vertical midplane $z/h = 0$.

thus diminishing the temperature difference between the cube surface and the fluid and consequently reducing heat removal. Hot spots migrate over the surface due to the local flow conditions and in particular unsteady flapping and meandering of the recirculation bubble behind the cube. This will generate unsteady thermal stresses in the cube which can cause thermal fatigue of the material. Hence, for good cooling of electronic components the removal of heat has to be strong but also as uniform as possible across all the faces of those components. Fig. 21 shows a time sequence of the cube surface temperature indicating several hot spots and their migration. Such an

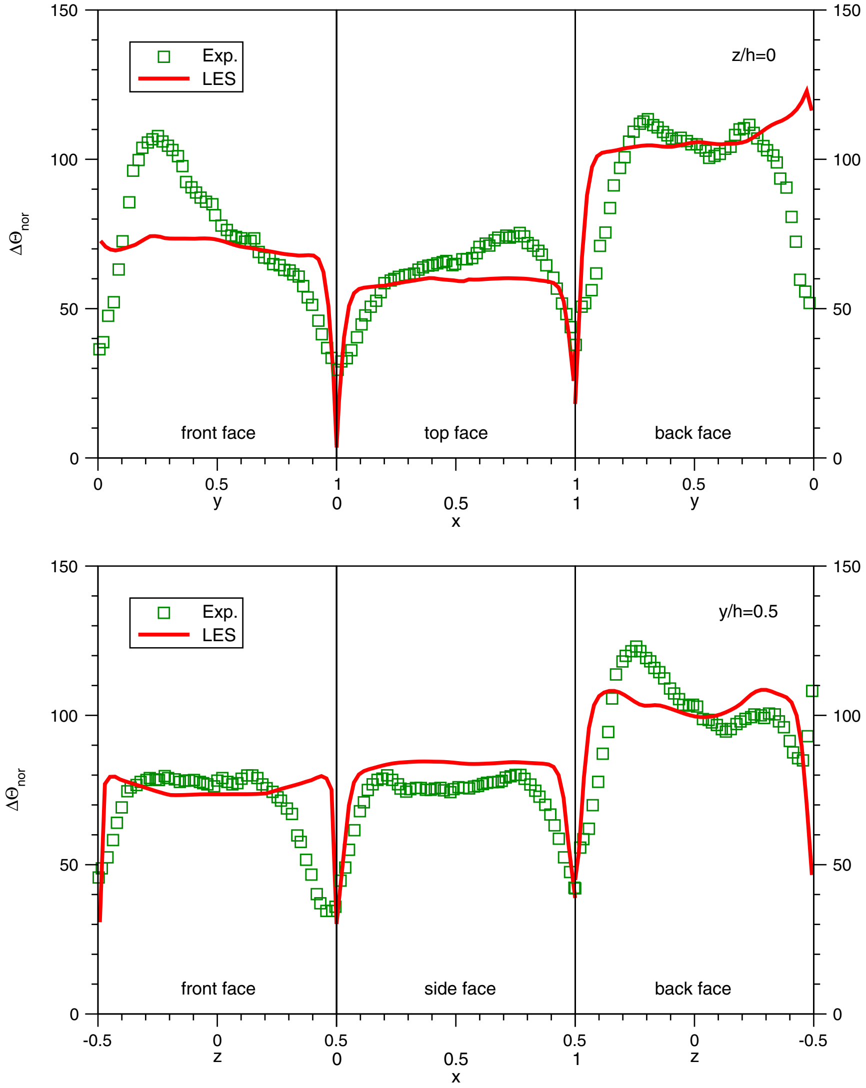

Fig. 19. Profiles of the normalised surface temperature difference along the pathline in the vertical midplane $z/h = 0$ (top) and the horizontal cutplane $y/h = 0.5$ (bottom).

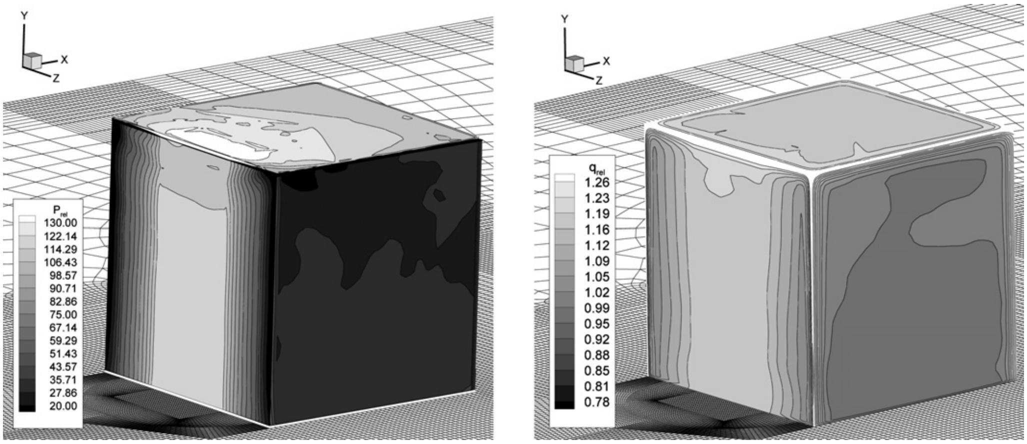

Fig. 20. Comparison between the averaged relative pressure (left) and heat flux (right) on the surface of the cube, which suggests the correlation between the two.

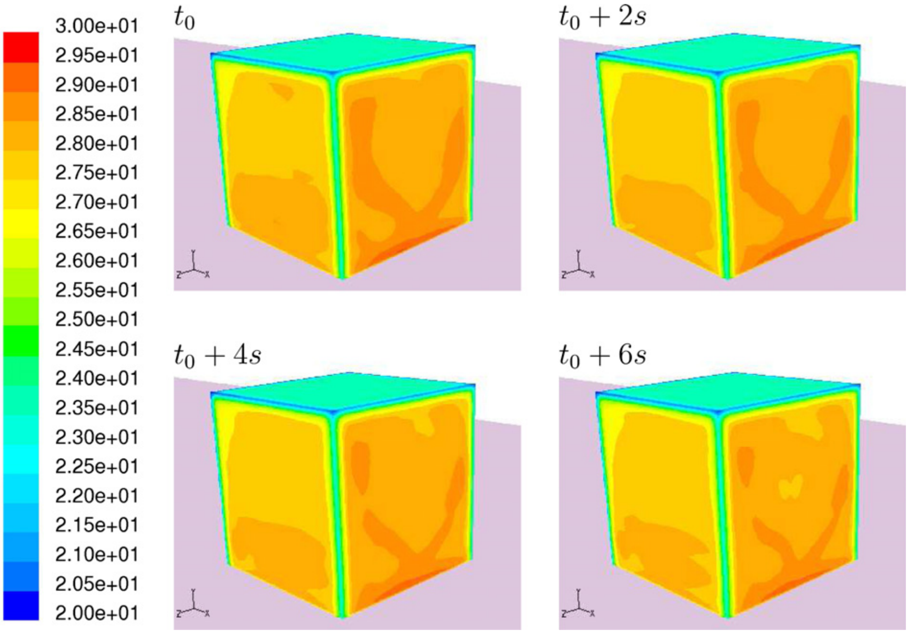

Fig. 21. Migration of the temperature hot spots on the side and the back of the cube, following the local flow pattern, presented by the time series of the instantaneous temperature contour plots (the view from the back).

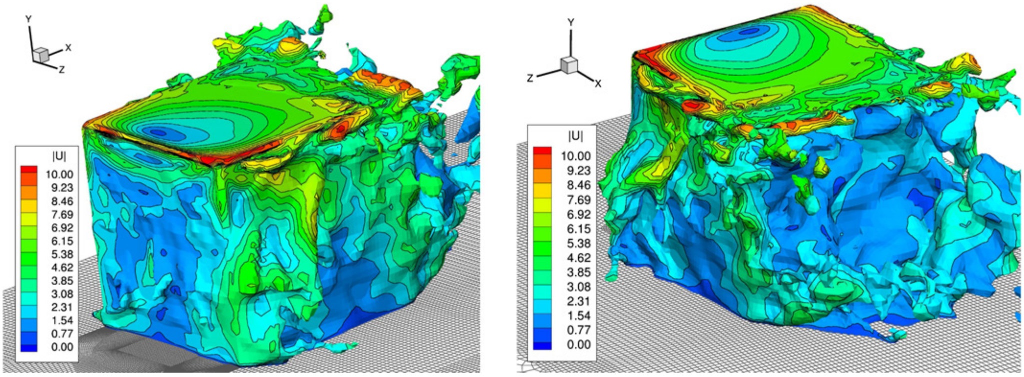

Fig. 22. Instantaneous temperature isosurface of $\Theta = 20.5$ °C, coloured with the velocity magnitude: the view from the front (left), and the view from the back (right).

information can be used for the control purposes, to prescribe the material and its thermal properties to suit the operating conditions and/or to design adequate cooling.

Finally, Fig. 22 shows two snapshots of a thermal plume around the cube, identified by the instantaneous temperature isosurface. The correlation with the velocity field is indicated by the imposed colour palette representing the velocity magnitude.

4. Conclusions

Large-eddy simulation of turbulent flow over a jet-impinged heated wall-mounted cube in a channel flow, despite relative geometric simplicity, showed to be quite a demanding test for the large-eddy simulations (LES). Despite relatively low Reynolds number, it required large computer resources, and involved significant work power to generate the mesh adequate for ensuring the desired resolution in several highly sheared flow zones. The LES here reported is believed to have satisfied the mesh resolution criteria, the numerical methods are all of second order accuracy, and the applied dynamic Smagorinsky subgrid-scale model provides adequate input from the unresolved motion. In all, the LES results presented are regarded as trustworthy and free of any serious numerical or modelling contamination. This claim is substantiated by relatively good agreement with the available experimental results. Nevertheless, some notable differences have been observed and symptomatically only in some flow regions. These differences have been identified and attributed partly to some unavoidable uncertainties in defining the inflow conditions, but more to a minor and yet influential geometrical difference between the experimental and LES configurations. The source of the noted discrepancy has been identified in the small shift of the jet centre as compared with the experiment, which led to about 10% difference in jet momentum splitting between the portion impinging on the cube top face and sweeping the cube front face. In view of the above, the here presented LES results can be considered on their own merit. Moreover, the LES configuration is easily reproducible and can serve as a reference test case for other computational methods, i.e. RANS and hybrid RANS/LES approaches.

The main outcome and conclusions of the analysis can be summarised as:

- The flow considered contains several generic events and phenomena, such as a cross-flow, intensive mixing, entrainment, impingement, separation, and vortical flow structures around the jet and the cube. The cross-flow exerts pressure which bends the jet, but also the interaction between the cross-flow and the jet determines the creation of the vortex rings which are generated in the shear region of the jet. The power density spectrum gave the characteristic frequency of these vortex rings $St = 0.81$, but also it showed the occurrence of higher harmonics, which come from the non-linearity in the interaction between the jet and the cross-flow.
- The jet, created from the flow through the orifice, contains a mild swirling motion, which is limited to the core of the jet and which extends all the way to the central cube. The cross-flow creates a horse shoe vortex that wraps around the jet and creates a recirculation zone behind it.
- The vortex rings that are travelling with the jet breakdown after hitting the surface of the central cube determining thus the characteristic frequency of the vortical structures around the cube. The lateral cross-flow creates a horse shoe vortex around the central cube and edge vortices on its sides, creating separation regions around and behind the cube. Together with the lateral cross-flow these structures contribute to the creation of an arch vortex behind the cube. The shear layer separating from the top face evolves into a Von Kármán vortex street behind the cube.
- From the results taken in the horizontal cutplane (Fig. 5) it could be seen that the obtained solutions are not fully symmetrical, although there is a full symmetry of the inflow and the boundary conditions. This, well acknowledged feature of a jet in a cross-flow, is in the present case even more pronounced because there is an interaction of a number of vortical structures of different scales originating either from the jet or from the channel (cross) flow over the cubes. A very long averaging time is, therefore, required to get a perfectly averaged field with symmetry. Note that even the experimental results of Tummers et al. (2005) are not fully symmetrical, as Fig. 5 clearly shows.
- As expected, there is a close relationship between the flow structures formed around the central cube and its cooling. The contours of the relative heat flux q_{rel} indicate the thermal activity on the surface of the cube and in the low-conducting envelope. The pattern of q_{rel} qualitatively corresponds to the pattern of the relative pressure difference P_{rel}, which in turn reflects the local velocity field. The best heat removal takes place on the cube top face, since it is entirely swept by the impinging fluid, as indicated by the characteristic jet streamlines. The upwind jet streamlines pass in front of the cube's leading edge, hence its front face is also flushed with the fresh fluid which increases the heat transfer. Only at the bottom of the front face, where the corner eddy is created, the cooling is somewhat reduced.
- The edge vortex establishes a diagonal flow stream across the cube's side face, which implies a constant influx of the cold fluid from the cross-flow towards that face that enhances the heat transfer. The least efficient heat removal takes place on the rear face of the cube. Due to the recirculation created behind the cube, the hot fluid stays trapped in that region and the heat transfer becomes very poor. Two vertical stripes of high temperature follow the legs of the arc vortex behind the cube. The highest temperatures on the cube surface are obtained at the bottom of the rear face, because this is the zone of very low velocities. The isosurface of the instantaneous fluid temperature, shown in Fig. 22, reflects the imprint of the vortical structures which contribute most to the heat removal from the cube.

Acknowledgements

The use of the supercomputer facilities at SARA was sponsored by the *National Computing Facilities Foundation* (NCF) with the financial support of the *Netherlands Organisation for Scientific Research* (NWO). A part of computations has also been performed using the supercomputer facilities at CINECA, sponsored by the EU project *HPC Europa* (Research Infrastructure Action, RII3-CT-2003-506079).

References

Calmet, I., Magnaudet, J., 1996. Large-eddy simulation of high-schmidt number mass transfer in a turbulent channel flow. Phys. Fluids 9, 438–455.

Geers, L.F.G. 2004. Multiple impinging jet arrays: an experimental study on flow and heat transfer. Ph.D. thesis, Delft University of Technology, Delft, The Netherlands.

Germano, M., Piomelli, U., Moin, P., Cabot, W.H., 1991. A dynamic subgrid-scale eddy viscosity model. Phys. Fluids A 3, 1760–1765.

Hadžiabdić, M. 2006. LES, RANS and combined simulation of impinging flows and heat transfer. Ph.D. thesis, Delft University of Technology, Delft, The Netherlands.

Hadžiabdić, M., Hanjalić, K., submitted for publication. Vortical structures and heat transfer in a round impinging jet.

Hanjalić, K., Popovac, M., Hadžiabdić, M., 2004. A robust near-wall elliptic relaxation eddy-viscosity turbulence model for CFD. Int. J. Heat Fluid Flow. 25, 897–901.

Kelso, R.M., Lim, T.T., Perry, A.E., 1996. An experimental study of round jets in a crossflow. J. Fluid Mech. 306, 111–144.

Meinders, E.R. 1998. Experimental study of heat transfer in turbulent flows over wall-mounted cubes. Ph.D. thesis, Delft University of Technology.

Moore, G., 1965. Cramming more components into integrated circuits. Electron. Mag. 38, 114–117.

Muppidi, S., Mahesh, K., 2005. Study of trajectories of jets in crossflow using direct numerical simulation. J. Fluid Mech. 530, 81–100.

Ničeno, B. 2001. An unstructured parallel algorithm for large eddy and conjugate heat transfer simulations. Ph.D. thesis, Delft University of Technology, Delft, The Netherlands.

Ničeno, B., Hanjalić, K., 2005. Unstructured large eddy and conjugate heat transfer simulations of wall bounded flows. In: Sunden, B., Faghri, M. (Eds.), Modelling and Simulation of Turbulent Heat Transfer. WIT Press.

Ničeno, B., Dronkers, A., Hanjalić, K., 2002. Turbulent heat transfer from a multilayered wall mounted cubes: a large eddy simulation. Int. J. Heat Fluid Flow 23, 173–185.

Popovac, M. 2006. Modelling and simulation of turbulence and heat transfer in wallbounded flows. Ph.D. thesis, Delft University of Technology, Delft, The Netherlands.

Rundström, D., Moshfegh, B., 2006. Investigation of flow and heat transfer of an impinging jet in a cross-flow for cooling of heated cube. Trans. ASME J. Electron. Packing 128, 150–156.

Shapiro, S., King, J., Closkey, R., Karagozian, A., 2006. Optimization of controlled jets in crossflow. AIAA J. 44, 1292–1298.

Tummers, M., Hanjalić, K., Rodnik, R., Flikweert, M., Moshfegh, B. 2005. Impinging jet cooling of wall mounted cubes. In: Rodi, W. (Ed.), Proceedings, ERCOFTAC/IAHR Symposium on Refined Flow Modelling.